COOL-LAMPS. Discovery of COOL J0335−1927, a Gravitationally Lensed Quasar at z = 3.27 with an Image Separation of 23″3

Kate Napier[1] , Michael D. Gladders[2,3] , Keren Sharon[1] , Håkon Dahle[4] , Aidan P. Cloonan[2] , Guillaume Mahler[5,6] ,
Isaiah Escapa[2] , Josh Garza[2] , Andrew Kisare[2] , Natalie Malagon[2] , Simon Mork[2] , Kunwanhui Niu[2] , Riley Rosener[2] ,
Jamar Sullivan, Jr.[2] , Marie Tagliavia[2] , Marcos Tamargo-Arizmendi[2] , Raul Teixeira[2] , Kabelo Tsiane[2] ,
Grace Wagner[2] , Yunchong Zhang[2] , and Megan Zhao[2]

[1] Department of Astronomy, University of Michigan, 1085 S University Ave, Ann Arbor, MI 48109, USA; kanapier@umich.edu
[2] Department of Astronomy and Astrophysics, University of Chicago, 5640 South Ellis Avenue, Chicago, IL 60637, USA
[3] Kavli Institute for Cosmological Physics, University of Chicago, 5640 South Ellis Avenue, Chicago, IL 60637, USA
[4] Institute of Theoretical Astrophysics, University of Oslo, P.O. Box 1029, Blindern, NO-0315 Oslo, Norway
[5] Centre for Extragalactic Astronomy, Durham University, South Road, Durham DH1 3LE, UK
[6] Institute for Computational Cosmology, Durham University, South Road, Durham DH1 3LE, UK
Received 2023 May 31; revised 2023 August 15; accepted 2023 August 16; published 2023 September 7

Abstract

We report the discovery of COOL J0335−1927, a quasar at $z = 3.27$ lensed into three images with a maximum separation of 23″3 by a galaxy cluster at $z = 0.4178$. To date, this is the highest redshift wide-separation lensed quasar known. In addition, COOL J0335−1927 shows several strong intervening absorbers visible in the spectra of all three quasar images with varying equivalent widths. The quasar also shows mini-broad line absorption. We construct a parametric strong gravitational lens model using ground-based imaging, constrained by the redshift and positions of the quasar images as well as the positions of three other multiply imaged background galaxies. Using our best-fit lens model, we calculate the predicted time delays between the three quasar images to be Δt_{AB} $= 499^{+141}_{-146}$ (stat) and $\Delta t_{AC} = -127^{+83}_{-17}$ (stat) days. Folding in systematic uncertainties, the model-predicted time delays are within the ranges $240 < \Delta t_{AB} < 700$ and $-300 < \Delta t_{AC} < -30$. We also present g-band photometry from archival Dark Energy Camera Legacy Survey and Pan-STARRS imaging, and new multi-epoch observations obtained between 2022 September 18 UT and 2023 February 22 UT, which demonstrate significant variability in the quasar and will eventually enable the measurement of the time delay between the three quasar images. The currently available light curves are consistent with the model-predicted time delays. This is the fifth paper from the COOL-LAMPS collaboration.

1. Introduction

To date, there are more than 300 quasars known to be gravitationally lensed into multiple images (Lemon et al. 2019, 2023). Most of these quasars are lensed by individual galaxies, resulting in separations of 1″–2″ between the lensed quasar images. There are only six published wide-separation lensed quasars (WSLQs), strongly lensed quasars in which the foreground lens is a group or cluster of galaxies, producing image separations >10″: Sloan Digital Sky Survey (SDSS) J1004+4112 (Inada et al. 2003); SDSS J1029 +2623 (Inada et al. 2006); SDSS J2222+2745 (Dahle et al. 2013); SDSS J0909+4449 (Shu et al. 2018); SDSS J1326 +4806 (Shu et al. 2019); and COOL J0542−2125 (Martinez et al. 2023).

Despite their rarity, WSLQs offer rich astrophysical insights due to the image separations and time delays that can be 1 magnitude larger than those produced by galaxy lenses. For example, the presence of a leading image ∼700 days ahead of the brightest images in SDSS J2222+2745 allowed Williams et al. (2021a, 2021b) to plan and execute a reverberation mapping campaign on this $z = 2.801$ WSLQ, providing the best constrained black hole mass currently available in the distant Universe. WSLQs can be used to study the quasar host galaxy (Ross et al. 2009; Cloonan et al. 2023), and interactions between the quasar and nearby gas, at a smaller scale than otherwise achievable (Bayliss et al. 2017). Since each lensed quasar image probes a slightly different line of sight, WSLQs can be used to construct the 3D spatial distribution of outflows (Misawa et al. 2013). WSLQs uniquely probe the mass distribution of the lens on a variety of scales (Liesenborgs et al. 2009; Oguri 2010; Oguri et al. 2013; Sharon et al. 2017; Forés-Toribio et al. 2022). Recently, Napier et al. (2023) presented a time-delay measurement of the Hubble parameter, H_0, based on the three best-studied WSLQs.

In this Letter, we present the discovery, spectroscopic confirmation, preliminary lens model, and photometric monitoring of COOL J0335−1927, a quasar at $z = 3.27$ strongly lensed by a galaxy cluster at $z = 0.4178$ into three images with maximum image separation of 23″3. Of all the known cluster-lensed quasars, this is the highest quasar redshift to date.

In Section 3, we present the ground-based spectroscopy, which confirms this target as a cluster-lensed quasar. We present an initial strong lensing model in Section 4. In Section 5, we present a prediction of the time delays between the quasar images. In Section 6, we present preliminary quasar light curves constructed from archival data and our new photometric monitoring campaign. We conclude in Section 7.

We assume a flat cosmology with $\Omega_\Lambda = 0.7$, $\Omega_m = 0.3$, and $H_0 = 70$ km s^{-1} Mpc^{-1}. In this cosmology, $1'' = 5.515$ kpc at
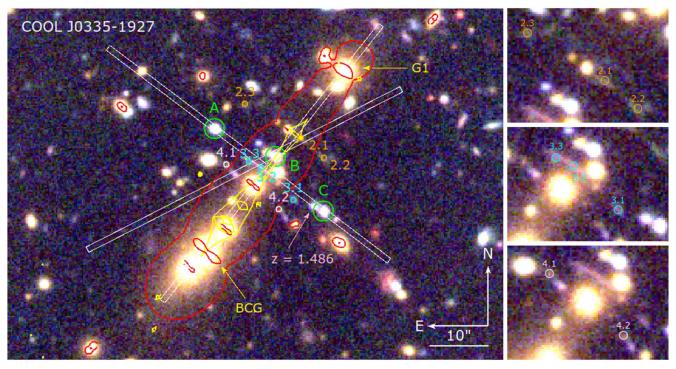
Figure 1. *grz* color composite imaging of COOL J0335−1927 from Magellan Telescopes LDSS3-C. The three quasar images are marked in green. The lensing critical curves, the points of maximum magnification for a source at a specified redshift, are computed at the quasar's redshift $z = 3.27$ and shown in red. Several other multiply imaged background sources are seen in the vicinity of the quasar images and are shown in the zoomed-in panels on the right. The white boxes mark the three LDSS3-C long-slit observations.

the cluster redshift, $z = 0.4178$, and $1'' = 7.495$ kpc at the source redshift, $z = 3.27$. Magnitudes are reported in the AB system unless otherwise stated.

2. Discovery

COOL J0335−1927 was discovered serendipitously by the COOL-LAMPS collaboration, as part of a systematic visual search for strong lenses (e.g., Khullar et al. 2021; Sukay et al. 2022; Zhang et al. 2023) in public imaging data from the Dark Energy Camera Legacy Survey (DECaLS; Dey et al. 2019). It was not flagged as a candidate WSLQ by the process described in Martinez et al. (2023) because two of the three lensed quasar images (images B and C) in COOL J0335−1927 are classified in the DECaLS Data Release 9 catalog as extended sources (Sérsic profiles). Much like the WSLQ SDSS J2222+2745 (Dahle et al. 2013), this system was found first due to the presence of arc-like features in survey images, which focused sufficient attention on the images to suggest the presence of three quasar images and trigger follow-up spectroscopy in 2022 September.

3. Data

3.1. Description of the Observations

We observed COOL J0335−1927 on 2022 September 17 with the LDSS3-C spectrograph on the Magellan 2 6.5 m Clay Telescope, with a total of three different long-slit positions, each time using the $1''0 \times 4'$ center long-slit dispersed by the volume phase holographic-all grism. The first and second slit positions, targeting the three candidate lensed quasar images, were observed for 2×900 s. The third slit position, targeting multiple apparent cluster lens galaxies, was observed for 900 s. Spectra were sky-subtracted, and wavelength- and

flux-calibrated using standard techniques in IRAF (Tody 1986, 1993). The seeing at the time of spectroscopic observations was $\sim 1''$.

On the same night, we also acquired *grz* imaging, totaling 600 s in the *z* filter, and 540 s in the *r* and *g* filters. We obtained additional *grz* imaging of COOL J0335−1927 on 2023 January 31, once again with the LDSS3-C instrument, with total integration times of 1200 s in the *z* filter, and 540 s in the *r* and *g* filters. The final stacked *grz* images have seeing of $0''85$, $0''65$, and $0''55$, respectively. A color image from these data is shown in Figure 1. Notably, the two quasar images classified as extended in the DECaLS catalogs are not obviously extended in these sharper and deeper data.

3.2. Results from Spectroscopy

The LDSS3-C spectra of the three quasar images confirm that they are indeed three images of the same background source, as shown in Figure 2. Based on the He I 1640 and C III lines, we derived a systemic quasar redshift of $z = 3.27$, which is, to date, the highest redshift of a quasar lensed by a galaxy cluster. The LDSS3-C $R \sim 550$ spectra (at 6000 Å) with a continuum signal-to-noise ratio of ~ 20 per resolution element show that all three quasar images have a significant number of absorption lines. Of particular note is a wide ($\sigma \sim 700$ km s^{-1}) and almost opaque absorption feature 290 km s^{-1} redward of the systemic velocity that classifies COOL J0335−1927 as a "mini"-broad absorption line (BAL) quasar (e.g., Barlow et al. 1997). There are also two foreground absorbers visible in the extant spectroscopy, at $z = 1.486$ and $z = 1.829$, the former of which corresponds to a galaxy in close projection to image C at the same redshift with a detected [O II] doublet in emission (see Figure 1). The three widely separated lensed quasar images each probe both the absorbing material around the quasar itself
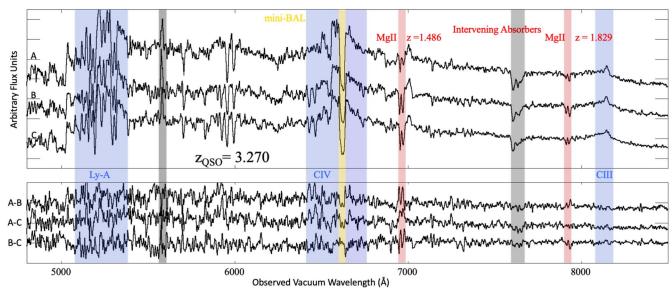
Figure 2. LDSS3-C spectra of the three quasar images of COOL J0335−1927. The spectra are vertically offset for clarity, with the top, middle, and bottom spectra corresponding to images A, B, and C, respectively. The gray shaded regions indicate major telluric and night sky features. The C III blue region was used to derive the systemic redshift. The system is classified as a "mini"-BAL quasar based on the broad and nearly opaque absorption seen redshifted relative to systemic at C IV. The red shaded regions indicate a Mg II absorption feature used to identify intervening absorbers at $z = 1.486$ (see also Figure 1) and at $z = 1.829$. The bottom panel shows the difference spectra of the three pairs of quasar images. The difference spectra are consistent with the noise. Future work will investigate any differences in the quasar spectra resulting from variability or line-of-sight differences due to intrinsic and intervening absorption.

Table 1
The Positions and Redshifts of the Multiple-image Systems in the COOL J0335−1927 Field

ID	R.A. [J2000]	Decl. [J2000]	z	μ	Δt (days)	rmsi ['']
QSO Image A	53.769891	−19.462959	3.27	$5.3^{+3.4}_{-1.8}$	…	0.09
QSO Image B	53.766807	−19.464290	3.27	$4.5^{+3.2}_{-1.7}$	499^{+141}_{-146}	0.28
QSO Image C	53.764431	−19.466858	3.27	$5.3^{+4.5}_{-1.5}$	-127^{+83}_{-17}	0.16
2.1	53.765563	−19.463420	$2.91^{+0.56}_{-0.28}$	...	...	0.19
2.2	53.764377	−19.464362	$2.91^{+0.56}_{-0.28}$	...	...	0.15
2.3	53.768347	−19.461810	$2.91^{+0.56}_{-0.28}$	...	...	0.13
3.1	53.765909	−19.466316	$1.29^{+0.22}_{-0.14}$	...	...	0.04
3.2	53.767522	−19.464820	$1.29^{+0.22}_{-0.14}$	...	...	0.35
3.3	53.768146	−19.464550	$1.29^{+0.22}_{-0.14}$	...	...	0.28
4.1	53.769297	−19.464671	$1.25^{+0.21}_{-0.12}$	...	...	0.20
4.2	53.766640	−19.466771	$1.25^{+0.21}_{-0.12}$	...	...	0.24

Note. The quasar images have a spectroscopic redshift z. Redshifts with error bars indicate the best-fit lens model-optimized redshift and the 1σ confidence interval. For the quasar images, the lens model-predicted magnifications and time delays and their 1σ errors from the MCMC sampling of the parameter space are listed. The rms scatters in the image plane between the observed image positions and the model-predicted positions are listed in the last column. The ground-based lens model is uncertain and the statistical error bars do not represent the true uncertainties, which are likely underestimated (e.g., see Figure 8 in Sharon et al. 2012).

and the intervening absorbers along different lines of sight, separated by impact parameters of tens of kpc for the foreground absorbers and on subparsec scales for the intrinsic absorption. Even at this modest resolution, there are apparent differences in equivalent widths between the foreground absorbers across the three quasar images—see, for example, the indicated foreground absorber at $z = 1.486$ in Figure 2; a more detailed analysis awaits higher resolution spectroscopy.

4. Lens Model

We computed an initial strong lensing model for the foreground galaxy cluster lens of COOL J0335−1927 from ground-based imaging and spectroscopy, using as constraints the positions of multiple images of lensed background sources (Table 1), and where available, their spectroscopic redshifts (currently, only the quasar).

The strong lensing model presented here was constructed using Lenstool (Jullo et al. 2007). This parametric modeling algorithm models the lens plane as a linear combination of mass halos. The mass halos represent the dark matter mass distribution from the cluster scale to the individual galaxy scale. We modeled each mass halo as a pseudo-isothermal ellipsoidal mass distribution (PIEMD or dPIE; Elíasdóttir et al. 2007), which has seven parameters: position (x, y); ellipticity $e = (a^2 - b^2)/(a^2 + b^2)$, where a and b are the semimajor and semiminor axes, respectively; position angle θ; core radius r_c; truncation radius $r_{\rm cut}$; and effective velocity dispersion σ_0.

In addition to the cluster-scale halo, the lens model assigns a mass distribution to each cluster member galaxy to account for their contribution to the lensing potential. For cluster-member selection, we obtained grz photometry for all the sources in the field from the Legacy Survey Data Release 9 catalog. Cluster

member galaxies were then identified using the red-sequence technique (Gladders & Yee 2000), by comparing their $g-r$ color to that of the cluster red-sequence in a color–magnitude diagram of $g-r$ versus r. Our lens model included 29 cluster member galaxies. The positional parameters of the galaxy-scale halos (x, y, e, θ) were fixed to the values we measured with Source Extractor (Bertin & Arnouts 1996) in the LDSS3-C r-band imaging data. This was done in order to fully exploit the depth of the LDSS3-C data, and obtain measurements of the cluster members in the same reference frame as the lensing constraints. The galaxy-scale σ_0, r_c, and r_{cut} parameters were scaled to their observed luminosity using the scaling relations in Limousin et al. (2005). The parameters of the cluster-scale halo, with the exception of r_{cut}, were allowed to vary. The cut radius for the cluster-scale halo was fixed to 1500 kpc because this parameter falls outside of the region where strong lensing occurs, and therefore, cannot be constrained. We constrained the x- and y-positions of the cluster-scale halo to be within $\pm 10''$ from the center of the brightest cluster galaxy (BCG) and set broad priors for the other free parameters.

A cluster member galaxy in the northwest (G1) contributes significant substructure to the lensing potential and likely marks an underlying dark matter subhalo. Thus, for this galaxy, we optimized the r_c, r_{cut}, and σ_0 parameters instead of adopting the values from the Limousin et al. (2005) scaling relations.

The best-fit lens model is defined as the one that minimizes the scatter between the observed and model-predicted image locations in the image plane. The best-fit model parameters and their 1σ errors from the MCMC sampling of the parameter space are as follows: for the cluster-scale halo, ΔR.A. $['']=-5.0^{+3.3}_{-1.5}$; Δdecl. $['']=6.7^{+1.8}_{-4.6}$; $e=0.57^{+0.13}_{-0.33}$; $\theta=51.9^{+0.02}_{-2.8}$ degrees; $r_c=80.6^{+15.2}_{-15.9}$ kpc; $r_{cut}=1500$ kpc (not optimized); and $\sigma_0=870^{+93}_{-112}$ km s^{-1}; and for G1, $r_c=7.3^{+1.0}_{-5.7}$ kpc; $r_{cut}=29.9^{+11.7}_{-12.7}$ kpc; and $\sigma_0=328^{+141}_{-25}$ km s^{-1}. For the scaling relations of galaxy-scale halos, the best-fit effective velocity dispersion was $\sigma_0^*=165^{+25}_{-23}$ km s^{-1}. The pivot truncation radius is poorly constrained between the priors of 20–150 kpc with a best-fit value of $r_{cut}^*=54.4$ kpc. Whereas the scaling relations produced $\sigma_0=177^{+27}_{-25}$ km s^{-1} for G1, the optimized value $\sigma_0=328^{+141}_{-25}$ km s^{-1} was significantly higher, which points to a possible existence of an underlying dark matter substructure. A more robust investigation of this component requires more lensing constraints and is reserved for future work. The coordinates ΔR.A. and Δdecl. are listed in arcseconds measured east and north of the reference [R.A., decl.] = [53.770260, −19.468757], the center of the BCG.

The lens model does not predict any additional lensed quasar images. The rms scatter in the image plane is $0''.21$. We find that the main cluster halo is generally aligned with the observed cluster light, that is, along the line connecting the few bright cluster member galaxies seen in Figure 1. The x- and y-positions of the main cluster halo are strongly correlated, and the lack of lensing constraints southeast of the BCG means that the position of the cluster-scale halo is underconstrained, allowing it to move freely in that direction.

Table 1 includes the model-predicted magnification of each of the lensed quasar images. We used our best-fit lens model to determine the mass density projected within 250 kpc of the BCG, and measure $M(<250\,\text{kpc})=1.44^{+0.27}_{-0.17}\times10^{14}M_\odot$.

The statistical uncertainties on the model outputs, i.e., the mass, magnification, and time delay, were derived from a set of 100 models, sampled from the MCMC chains. We note that the

statistical modeling uncertainties underestimate the true uncertainty, as systematic uncertainties due to modeling choices, image identification, and lack of constraints can be significant (e.g., Johnson & Sharon 2016). To obtain a better handle on systematic uncertainties and their implications, we computed several test models with different modeling assumptions, including removing constraints from the other multiply imaged background sources, removing the faintest magnitude of cluster member galaxies, and using a Navarro–Frenk–White profile for the main halo instead of a PIEMD halo. We also experimented with fixing the free parameters of G1 if the number of free parameters exceeded the number of constraints. We find that overall the resulting test models are consistent with our "fiducial" model in terms of the predicted magnification and time delay outputs, where constraints are available, albeit with larger uncertainties. As noted above, the position of the main cluster halo is poorly constrained. As a result, the best-fit cluster halo position varied significantly between test models by more than the implied in-model statistical uncertainty. The results presented hereafter are reported for our "fiducial" lens model, while the test models were used to inform the reported uncertainties.

5. Predicted Time Delay

Because quasars vary in brightness over time, the time delay between the multiple lensed images of the quasar can be determined. Time delays between images of variable lensed sources can be used for measuring the Hubble constant (e.g., Wong et al. 2020; Kelly et al. 2023; Napier et al. 2023), and are necessary for interpreting temporal and spatial variations in the intrinsic quasar absorption lines, which can then be used to probe the 3D structure of material near the quasar (Misawa et al. 2016).

Once the lensing potential is known, the time delay between images of a lensed source can be calculated from the excess arrival time surface (Schneider 1985):

$$t(\boldsymbol{\theta}, \boldsymbol{\beta}) = \frac{1+z_l}{c}\frac{d_l d_s}{d_{ls}}\left[\frac{1}{2}(\boldsymbol{\theta}-\boldsymbol{\beta})^2 - \psi(\boldsymbol{\theta})\right], \qquad (1)$$

where z_l is the lens redshift, d_l, d_s, and d_{ls} are angular diameter distances from the observer to the lens, to the source, and between the lens and the source, respectively; $\boldsymbol{\theta}$ is the image position in the image plane; $\boldsymbol{\beta}$ is the unobserved source position; and $\psi(\boldsymbol{\theta})$ is the gravitational lensing potential. The last term, $\frac{1}{2}(\boldsymbol{\theta}-\boldsymbol{\beta})^2 - \psi(\boldsymbol{\theta})$, is also known as the Fermat potential.

Figure 3 shows the predicted excess arrival time surface in days, with respect to image A of the quasar, $\Delta t = t(\boldsymbol{\theta}, \boldsymbol{\beta}) - t(\boldsymbol{\theta}_A, \boldsymbol{\beta})$, derived from the best-fit lens model. Multiple images of a strongly lensed background source would appear at stationary points (minimum, maximum, and saddle points) in this potential; in the case of COOL J0335−1927, we observe two minima and a saddle point, resulting in three images of the lensed quasar.

The arrival time surface is very sensitive to small changes in the source position $\boldsymbol{\beta}$. We obtained the quasar source position $\boldsymbol{\beta}$ by averaging the predicted source positions from all three lensed quasar images. We calculated the time delays at the observed positions of the quasar images. The best-fit model-predicted time delays are $\Delta t_{AB} = 499^{+141}_{-146}$ days and $\Delta t_{AC} = -127^{+83}_{-17}$ days (statistical uncertainties). To assess

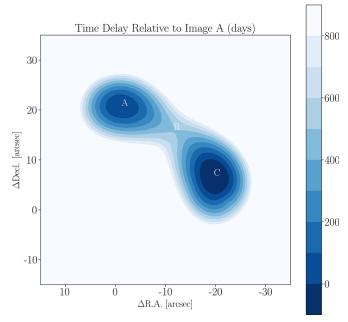**Figure 3.** The excess arrival time surface for light that is emitted from the quasar source position β at the source plane redshift $z = 3.27$ and passes the lens plane at $z = 0.4178$. We calculated the excess arrival time, which is reported in days, relative to image A of the quasar.
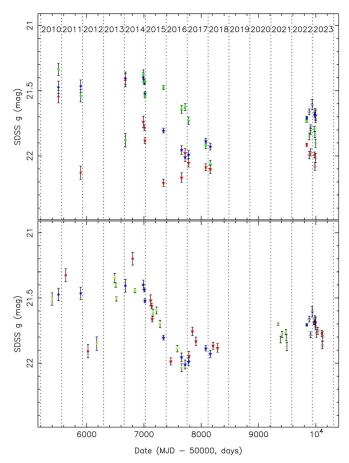

Figure 4. Top: the light curves of the quasar images A (blue), B (green), and C (red). The data points are aperture-photometry from Pan-STARRS (filled circles), DECaLS (filled stars), the Magellan Telescopes (filled squares), and the Nordic Optical Telescope (open circles). Bottom: the light curves for images B and C are shifted relative to image A by $\Delta t_{AB} = 499$ and $\Delta t_{AC} = -127$ days, the predicted time delays from the best-fit lens model. The data points of images B and C were then shifted vertically by 0.03 and 0.22 mag, respectively, to align with the light curve of image A (see Section 6).

the systematic uncertainties, we calculated the predicted AB and AC time delays for the various test models (see Section 4). The test models produced AB and AC time delays in the range of $240 < \Delta t_{AB} < 700$ and $-300 < \Delta t_{AC} < -30$. The statistical uncertainties likely underestimate the "true" uncertainties by a factor of ~ 2. The lens model is underconstrained, and space-based imaging data would significantly improve the robustness of the time-delay predictions by providing better resolution and new constraints.

6. Initialization of Photometric Monitoring

Photometric monitoring of COOL J0335−1927 is essential for measuring the observed time delays between the multiple images of the lensed quasar. We initiated photometric monitoring of COOL J0335−1927 in 2022 September. To date, we have obtained eight epochs of images in the g band utilizing the Magellan Telescopes and the 2.56 m Nordic Optical Telescope (NOT). We supplemented our new observations with archival data from Pan-STARRS (Flewelling et al. 2020), spanning three epochs from late 2010 to early 2014, and from DECaLS, spanning nine epochs between late 2014 and early 2018, to construct preliminary quasar light curves (top panel of Figure 4). The quasar images already show significant variability over time; e.g., the brightness of image A decreased by 0.6 magnitudes over a time span of 2 yr between late 2014 and late 2016, followed by a similar decline in image B. The light curves also show that the relative order of brightness of the images has changed. The data points from 2015 to 2016 show image B as significantly brighter than image A, whereas the opposite is true in our most recent photometric data from 2023. The DECaLS and Pan-STARRS g-band photometry show a decline in image C around (MJD-50000) ~ 7000 days, followed by subsequent declines in image A and, finally image B, which is consistent with the model-predicted order of the time delays provided in Section 5.

We shifted the light curves for images B and C in time relative to image A by the predicted time delays from the best-fit lens model (bottom panel of Figure 4). Furthermore, to visually match the light curve of image A, we also shifted the light curves for images B and C by 0.03 and 0.22 mag, respectively, relative to image A. The predicted time delays are consistent with the preliminary light curves. The predicted magnification ratios, however, are too uncertain to definitively say whether they are in agreement with the magnitude offsets applied to the shifted light curves.

While the data in hand, which sparsely sample a ~ 12 yr baseline, are not yet sufficient for obtaining robust time delays, the observed variability in the g band guarantees that such a measurement will be feasible. Higher-cadenced monitoring for this purpose will be implemented at NOT from 2023 August. Furthermore, COOL J0335−1927 is located within the LSST footprint of the Vera C. Rubin Observatory, which ensures high-quality light curves will be available in the near future.

7. Summary and Conclusions

This paper presents the discovery, spectroscopic confirmation, and preliminary photometric light curves of COOL J0335−1927, a wide-separation lensed quasar at $z = 3.27$; and a

preliminary strong lens model, which we computed based on the available ground-based multiband imaging and spectroscopy. We used the best-fit lens model to make preliminary predictions of the time delays between the three images of the lensed quasar, which are qualitatively consistent with the quasar image light curves available to date. We demonstrated that the high variability, which is already observed in the archival and newly obtained imaging, all but guarantees that an accurate measurement of the observed time delays will be feasible once sufficient data are collected.

Our discovery and spectroscopic confirmation of COOL J0335−1927 increases the small, but scientifically valuable sample of WSLQs. These unique systems enable a broad array of studies ranging from the nature of quasars and their hosts, through the properties of the foreground structures that lens them, to the expansion rate of the Universe itself. The preliminary results presented here offer a glimpse into COOL J0335−1927, an interesting target whose analysis has just begun.

ORCID iDs

Kate Napier ⓘ https://orcid.org/0000-0003-4470-1696
Michael D. Gladders ⓘ https://orcid.org/0000-0003-1370-5010
Keren Sharon ⓘ https://orcid.org/0000-0002-7559-0864
Håkon Dahle ⓘ https://orcid.org/0000-0003-2200-5606
Aidan P. Cloonan ⓘ https://orcid.org/0000-0001-9978-2601
Guillaume Mahler ⓘ https://orcid.org/0000-0003-3266-2001
Isaiah Escapa ⓘ https://orcid.org/0000-0003-0896-8502
Josh Garza ⓘ https://orcid.org/0009-0007-1440-1832
Andrew Kisare ⓘ https://orcid.org/0009-0006-7664-877X
Natalie Malagon ⓘ https://orcid.org/0000-0002-5825-7795
Simon Mork ⓘ https://orcid.org/0000-0002-5573-9131
Kunwanhui Niu ⓘ https://orcid.org/0009-0001-5944-5624
Riley Rosener ⓘ https://orcid.org/0000-0001-7905-2134
Jamar Sullivan, Jr. ⓘ https://orcid.org/0009-0000-9780-4328
Marie Tagliavia ⓘ https://orcid.org/0000-0002-6832-4680
Marcos Tamargo-Arizmendi ⓘ https://orcid.org/0009-0008-0518-8045
Raul Teixeira ⓘ https://orcid.org/0000-0002-5279-0230
Kabelo Tsiane ⓘ https://orcid.org/0009-0008-6557-2065
Grace Wagner ⓘ https://orcid.org/0000-0003-0295-875X
Yunchong Zhang ⓘ https://orcid.org/0000-0001-6454-1699
Megan Zhao ⓘ https://orcid.org/0009-0006-4143-1159

References

Barlow, T. A., Hamann, F., & Sargent, W. L. W. 1997, in ASP Conf. Ser. 128, Mass Ejection from Active Galactic Nuclei, ed. N. Arav, I. Shlosman, & R. J. Weymann (San Francisco, CA: ASP), 13
Bayliss, M. B., Sharon, K., Acharyya, A., et al. 2017, ApJL, 845, L14
Bertin, E., & Arnouts, S. 1996, A&AS, 117, 393
Cloonan, A., Khullar, G., Napier, K., et al. 2023, AAS Meeting Abstracts, 55, 301.10
Dahle, H., Gladders, M. D., Sharon, K., et al. 2013, ApJ, 773, 146
Dey, A., Schlegel, D. J., Lang, D., et al. 2019, AJ, 157, 168
Elíasdóttir, Á., Limousin, M., Richard, J., et al. 2007, arXiv:0710.5636
Flewelling, H. A., Magnier, E. A., Chambers, K. C., et al. 2020, ApJS, 251, 7
Forés-Toribio, R., Muñoz, J. A., Kochanek, C. S., & Mediavilla, E. 2022, ApJ, 937, 35
Gladders, M. D., & Yee, H. K. C. 2000, AJ, 120, 2148
Inada, N., Oguri, M., Morokuma, T., et al. 2006, ApJ, 653, L97

Inada, N., Oguri, M., Pindor, B., et al. 2003, Natur, 426, 810
Johnson, T. L., & Sharon, K. 2016, ApJ, 832, 82
Jullo, E., Kneib, J.-P., Limousin, M., et al. 2007, NJPh, 9, 447
Kelly, P. L., Rodney, S., Treu, T., et al. 2023, Science, 380, abh1322
Khullar, G., Gozman, K., Lin, J. J., et al. 2021, ApJ, 906, 107
Lemon, C., Anguita, T., Auger-Williams, M. W., et al. 2023, MNRAS, 520, 3305
Lemon, C., Auger, M. W., & McMahon, R. G. 2019, MNRAS, 483, 4242
Liesenborgs, J., de Rijcke, S., Dejonghe, H., & Bekaert, P. 2009, MNRAS, 397, 341
Limousin, M., Kneib, J.-P., & Natarajan, P. 2005, MNRAS, 356, 309
Martinez, M. N., Napier, K. A., Cloonan, A. P., et al. 2023, ApJ, 946, 63
Misawa, T., Inada, N., Ohsuga, K., et al. 2013, AJ, 145, 48
Misawa, T., Saez, C., Charlton, J. C., et al. 2016, ApJ, 825, 25
Napier, K., Sharon, K., Dahle, H., et al. 2023, arXiv:2301.11240
Oguri, M. 2010, PASJ, 62, 1017
Oguri, M., Schrabback, T., Jullo, E., et al. 2013, MNRAS, 429, 482

Ross, N. R., Assef, R. J., Kochanek, C. S., Falco, E., & Poindexter, S. D. 2009, ApJ, 702, 472
Schneider, P. 1985, A&A, 143, 413
Sharon, K., Bayliss, M. B., Dahle, H., et al. 2017, ApJ, 835, 5
Sharon, K., Gladders, M. D., Rigby, J. R., et al. 2012, ApJ, 746, 161
Shu, Y., Koposov, S. E., Evans, N. W., et al. 2019, MNRAS, 489, 4741
Shu, Y., Marques-Chaves, R., Evans, N. W., & Pérez-Fournon, I. 2018, MNRAS, 481, L136
Sukay, E., Khullar, G., Gladders, M. D., et al. 2022, ApJ, 940, 42
Tody, D. 1986, Proc. SPIE, 627, 733
Tody, D. 1993, in ASP Conf. Ser. 52, Astronomical Data Analysis Software and Systems II, ed. R. J. Hanisch, R. J. V. Brissenden, & J. Barnes (San Francisco, CA: ASP), 173
Williams, P. R., Treu, T., Dahle, H., et al. 2021a, ApJ, 911, 64
Williams, P. R., Treu, T., Dahle, H., et al. 2021b, ApJL, 915, L9
Wong, K. C., Suyu, S. H., Chen, G. C. F., et al. 2020, MNRAS, 498, 1420
Zhang, Y., Manwadkar, V., Gladders, M. D., et al. 2023, ApJ, 950, 58